Hybrid silicon modulators

Invited Paper

Hui-Wen Chen, Yinghao Kuo, and J. E. Bowers*

Department of Electrical and Computer Engineering, University of California Santa Barbara, Santa Barbara, CA 93106, USA

**E-mail: bowers@ece.ucsb.edu*

Received January 13, 2009

A number of active elements have been demonstrated using the hybrid silicon evanescent platform, including lasers, amplifiers, and detectors. In this letter, two types of hybrid silicon modulators, fulfilling the building blocks in optical communication on this platform, are presented. A hybrid silicon electroabsorption modulator, suitable for high speed interconnects, with 10-dB extinction ratio at −5 V and 16-GHz modulation bandwidth is demonstrated. In addition, a hybrid silicon Mach-Zehnder modulator utilizing carrier depletion in multiple quantum wells is proved with 2 V·mm voltage-length product, 150-nm optical bandwidth, and a large signal modulation up to 10 Gb/s.

OCIS codes: 250.7360, 250.0250, 250.6715, 230.2090, 230.4205, 200.4650.

doi: 10.3788/COL20090704.0280.

Silicon-based modulators have attracted much attention with devices reported using free carrier plasma dispersion in Mach-Zehnder interferometric (MZI) form[1,2] or with a ring resonator structure[3,4] to increase the interaction of light with the active material. Silicon Mach-Zehnder modulators (MZMs) are generally less efficient with a modulation efficiency of 20 to 50 V·mm, which translates to longer interaction length and larger driving voltage. Both characteristics are less desirable for cost of the size and complicated design of high voltage complementary metal oxide semiconductor (CMOS) circuits. While ring resonator type modulators reduce the size, they also increase the sensitivity to temperature and decrease the operational optical bandwidth. InP-based electro-absorption modulators (EAMs) have shown small footprint and decent modulation efficiency at low driving voltage and have been widely used to make electro-absorption modulated lasers (EMLs) for high speed data communication. Recently, it has been reported that strained silicon also exhibits linear electro-optic refractive index modulation[5] and EAM on silicon has been demonstrated based on the Franz-Keldysh effect in strained SiGe[6,7]. However, the absorption coefficient in SiGe multiple quantum well (MQW) is still lower than InP-based MQWs. The additional absorption caused by the indirect band gap of Ge also introduces higher propagation loss at zero bias. We have demonstrated a new approach of integration of modulators into silicon using the wafer bonded hybrid silicon evanescent platform. Our EAM exhibits 5-dB extinction ratio (ER) at 10 Gb/s with sub-volt driving voltage, which makes it suitable using low power CMOS driving circuit. It can also be integrated with lasers, amplifiers, and photodetectors using quantum well intermixing[8] to make high speed integrated transceivers. To realize broadband optical switching and efficient phase modulation, we also developed a novel MZM utilizing carrier depletion in offset MQWs. Our MZM has a small footprint shorter than 1 mm and modulation efficiency of 2 V·mm. It is capable of modulation speed up to 10 Gb/s.

The basic structures of EAM and MZM modulators are similar except for the active region. A cross section of the hybrid modulator is illustrated in Fig. 1(a), which consists of III-V epitaxial layers bonded to silicon waveguides fabricated on a silicon on insulator wafer. Two 60-μm hybrid tapers, laterally tapered in both silicon and III-V layers, are used to minimize reflection and mode mismatch loss through adiabatically transforming the optical mode from pure silicon waveguide to the hybrid section. The InP cladding mesa is 4 μm wide while the quantum well (QW) and separate confinement heterostructure (SCH) layers are undercut to reduce the total device capacitance[9]. Silicon waveguides are fabricated with a waveguide height of 0.48 μm and slab height of 0.24 μm for the MZM. For the EAM, a silicon height of 0.6 μm is chosen to keep a similar confinement factor. The width of the waveguide is 1 μm in the hybrid section and 1.5 μm in passive regions.

The electrode design of high speed operation for EAM and MZM differs from each other since the MZM requires a longer modulation section. In general, the EAM has a very small footprint around 100 μm such that the device can be easily operated above 10 GHz with careful design

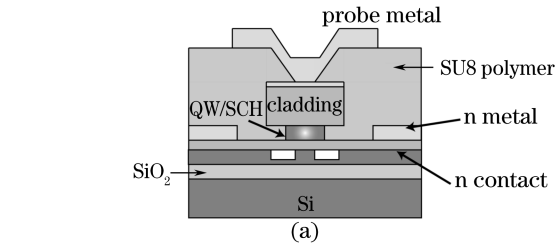

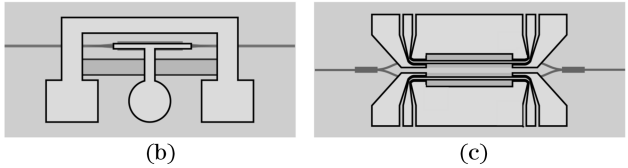

Fig. 1. (a) Cross section of both EAM and MZM at the hybrid section; (b) schematic top view of an EAM; (c) schematic top view of a MZM.

of the active region to control the overall resistance-capacitance (RC) cut-off frequency. Figure 1(b) shows the top view of a single EAM with simple direct current (DC) probe pads for both p and n contacts. In contrast, the length of a MZM has to be at least 500 μm to introduce enough phase shift. Therefore, it is important to utilize traveling wave electrodes (TWEs) for electrical signal propagation to overcome the RC limitation. A MZM with coplanar waveguide (CPW) as the TWE is depicted in Fig. 1(c) to realize high speed performance up to 10 Gb/s.

AlGaInAs is chosen as the MQW material for the silicon evanescent EAM because it has a larger conduction band offset, ΔE_c, which provides a stronger carrier confinement and produces a strong quantum confined Stark effect (QCSE) with higher ER[9]. The MQW section contains 10 wells and 11 barriers with the photoluminescence (PL) peak at 1478 nm. SCH layers with band gap equal to 1.3 μm are added both on top of and below the MQW region. The top SCH is slightly doped to assure most of the voltage drop across MQW, while the bottom SCH remains undoped to prevent dopant diffusion from highly doped n-InP and also help reducing overall capacitance.

For silicon evanescent MZM and switch, the PL peak of the MQW is designed at 1.36 μm to ensure low absorption at the operating wavelength (1.55 μm). Both the top SCH layer and MQW are doped in order to introduce free carriers[10]. The thickness and doping of the top SCH layer are carefully designed such that it can be completely depleted in the absence of an externally applied electric field. Thus, all the applied bias voltage will be used to deplete carriers in the MQW region rather than in the SCH layer. The compositions of wells and barriers are chosen to have shallower ΔE_c compared with EAMs and lasers to enhance the band-filling effect.

Once the carriers start to deplete out of the MQW, several physical effects, such as band-filling, plasma, Pockels, and Kerr effects, all contribute to the index change. Among them, the Pockels effect is the only phenomenon which is sensitive to crystal orientation. In other words, this effect can be additive to other effects if the optical signal propagates along the right direction. Otherwise the Pockels effect will introduce index change opposite to other effects. On the hybrid silicon platform, the direction of patterned silicon waveguide needs to be aligned to the [011] plane of the III-V material so that the phase shift is the maximum. Figure 2 shows the simulation results with consideration of all these effects[11−13]. As can be seen, the index change is proportional to the magnitude of the reverse bias. Moreover, the introduced index shift with orientation match is approximately 1.5 times larger than the mismatch case.

The silicon evanescent device fabrication flow consists of silicon waveguide formation, low temperature wafer bonding, and post-bonding fabrication. In this work, we used a bonding technique utilizing vertical outgassing channels (VOCs)[14] for 3 h at 300 °C. The array of 6×6 (μm) VOCs with 50-μm spacing assists in quenching H_2 outgassing during bonding.

After bonding, the mesa structure is fabricated using a self-aligned dry etching process[15]. A stack of Pd/Ti/Pd/Au p-contacts and a thin layer of silicon nitride is used as the hard mask for reactive ion etching (RIE) to form a 4-μm-wide mesa. A selective wet etching is then applied to create the undercut while several circular patterns with different radii are laid out on the mask to monitor and control the distance of the undercut. The sample is then dipped into diluted HCl to remove native indium oxide on the sidewall of the QW/SCH layers to avoid current leakage before depositing silicon nitride for passivation. After forming n-contacts with a Ni/Au/Ge/Ni/Au metal stack, the device is annealed with a resistive heater for 30 s. A 5-μm-thick polymer is coated to provide additional mechanical support for the thin bonding layer and to keep the TWE away from the underlying ground in order to reduce the impedance mismatch and to minimize parasitic capacitances.

For an EAM, the absorption shift due to QCSE can be observed by measuring the photocurrent at different wavelengths, as shown in Fig. 3. The device under test has a 100-μm-long absorber and the optical input power is kept at 0.5 mW across all wavelengths. The absorption edge shifts by about 20 nm for each additional volt applied to the device. Figure 4 shows the relative ER at 1550 nm under various reverse biases. More than 10-dB ER can be achieved with less than 4-V bias for 100-μm-long devices. For a longer device with a 250-μm absorber, it only takes 2.5 V to achieve 10-dB ER. The propagation loss of the hybrid waveguide was found to be around 3.6 dB/mm by measuring the device loss with different absorber lengths, as shown in Fig. 5. A pair of cascade EAMs reversely biased at 5 V are used to measure the on-chip loss of the fabricated 100-μm EAM. The on-chip loss is around 3 dB mainly due to the excess loss from both tapers.

The experimental data of the first demonstrated MZM

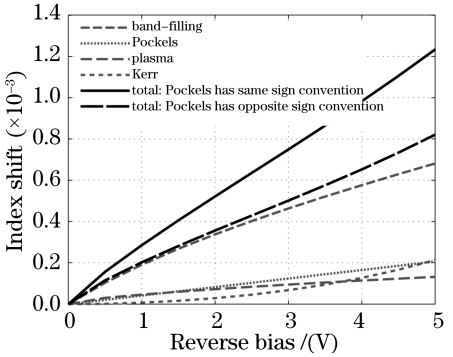

Fig. 2. Estimated index shift of a carrier depletion phase modulator in InAlGaAs MQW.

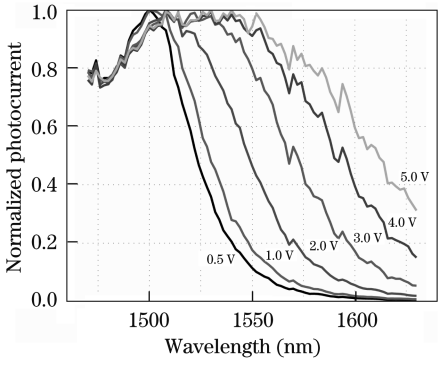

Fig. 3. Photocurrent at different bias voltages.

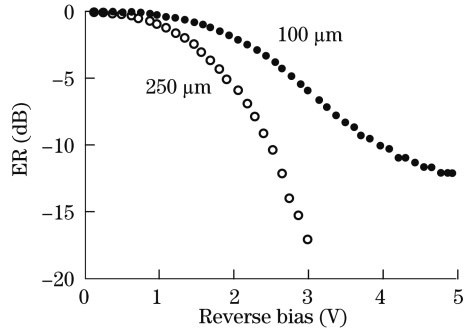

Fig. 4. ER at 1550 nm for 100- and 250-μm-long EAMs.

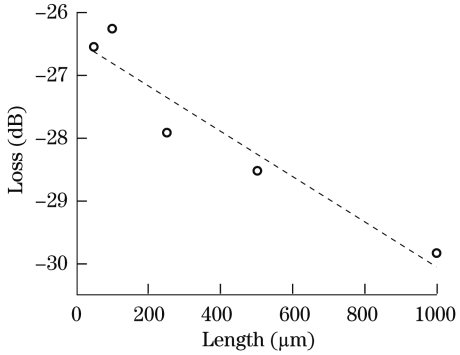

Fig. 5. Results of cutback measurement for device propagation loss.

is shown in Fig. 6. The device is biased from 0 to −5 V at one arm while the other arm is kept grounded. The voltage needed for π phase shift is then calculated using the transmission curve. As can be seen, the voltage-length product $V_\pi L$ is around 4 V·mm at 1550 nm and varies from 2 to 6 V·mm over entire S band, C band, and L band. The optical bandwidth of such a device is 150 nm for the ER larger than 9 dB. Since the bonding orientation was not considered during the period of fabrication, the Pockels effect has a sign convention different from other physical effects as mentioned above. Therefore the V_π deviates from the best estimation, but still stays consistent with the theoretical calculation. Meanwhile the ER is now limited by loss imbalance as a result of QCSE, which is more obvious at the bias voltage larger than −3 V. This effect will introduce additional loss, change the optical amplitude of the bias arm, and result in worse ER. In the future, this problem can be

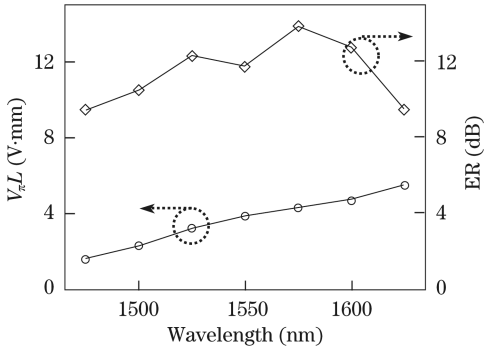

Fig. 6. Voltage-length product $V_\pi L$ and ER of a 1-mm MZM from 1475 to 1625 nm.

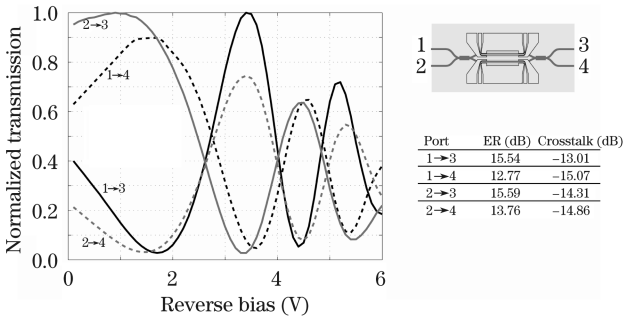

Port	ER (dB)	Crosstalk (dB)
1→3	15.54	−13.01
1→4	12.77	−15.07
2→3	15.59	−14.31
2→4	13.76	−14.86

Fig. 7. Transmission of a switch as a function of reverse bias with 12.5-dBm optical input power.

solved by introducing a π phase difference between two arms at zero bias by using a heater or laying out different path lengths.

Additionally, the hybrid silicon switch is also of interest for such a MZI based structure. In order to implement a switch, the passive silicon 1×2 multimode interference (MMI) is replaced by a 2×2 MMI. The all-port transmission as a function of reverse bias of this 2×2 switch is shown in Fig. 7, where $V_\pi L$ is around 1.5 V·mm. This device has better voltage-length product because the crystal orientations between the III-V epitaxial layer and the silicon waveguide are carefully aligned, where the Pockels effect adds up with other physical effects. The minimum ER is 12.77 dB and the maximum crosstalk is −13 dB, as shown also in Fig. 7.

To investigate the high speed performance of the devices, the frequency response of both EAM and MZM are measured using a HP 8730 lightwave component analyzer. As shown in Fig. 8(a), two 100-μm-long EAMs with different MQW undercuts are measured. The device with 3-μm-wide MQW section has a series resistance around 30 Ω and capacitance of 0.2 pF at 2-V bias, which corresponds to a cut-off frequency around 10 GHz. The modulators are also driven with a $2^{31}-1$ pseudorandom bit sequence (PRBS) to explore the performance of large signal modulation. The modulated light is collected with a lensed fiber and amplified with an erbium-doped fiber amplifier (EDFA). A 100-GHz filter is used to reduce the amplified spontaneous emission (ASE) noise before the signal is detected by a 30-GHz photodetector and sampled using an Agilent digital communication analyzer (DCA). Peak-to-peak driving voltage of 0.82 V is used to produce the clear eye diagram with 5-dB ER. We can further improve the speed with a more aggressive MQW undercut. The device with 2-μm-wide MQW section drops the capacitance to around 0.1 pF and produces a 3-dB bandwidth over 16 GHz. The downside is the reduction of the MQW volume, which leads to the increase of driving voltage. The open eye diagram with 6-dB ER is taken with much higher voltage swing of 3.2 V (peak-to-peak). The aggressive selective etching is also capable of over-etching under the taper section which results in higher insertion loss and lower yields. After increasing the reverse bias to 4 V, the EAM turns to be an efficient photodetector with on-chip responsivity greater than 0.8 A/W and bandwidth over 4.5 GHz. The reductions of speed performance for the detectors are mainly due to the excessive MQW region under the taper section which results in slow diffusion carriers. Estimated photo-carrier

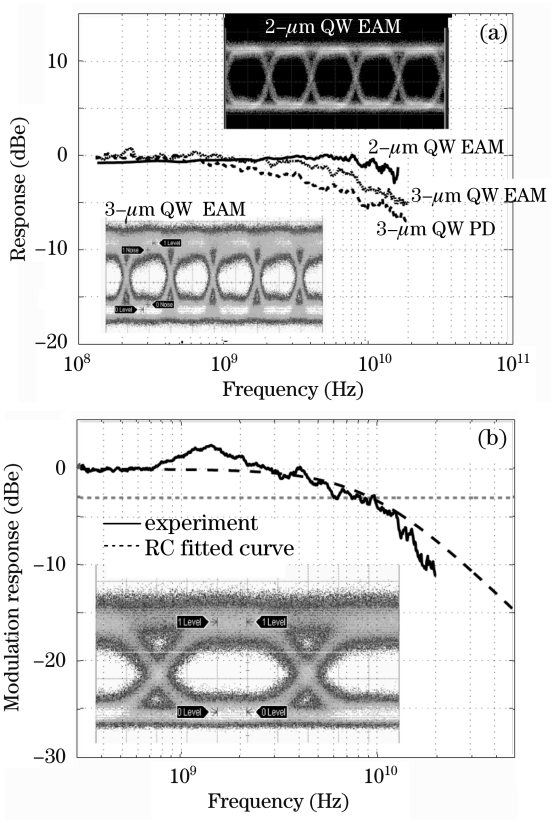

Fig. 8. (a) Response curves of two 100-μm-long EAMs with different MQW section widths of 2 and 3 μm. The response of a photodetector (PD) is also given. Insets show the eye diagrams. (b) Frequency response and RC fitted estimation of MZM. Inset is the 10-Gb/s eye diagram.

generated in the taper region is about 10% of the total photocurrent.

Similar to the EAM, the frequency response of a MZM is shown in Fig. 8(b). Since the length of a MZM is longer than that of an EAM, it is expected that the RC cut-off frequency is lower. Hence a CPW TWE is applied on the device to improve the modulation bandwidth as mentioned previously. The measurement is performed with a 25-Ω termination to reduce the reflection from the open end of the TWE. This termination introduces a resonance at 1.5 GHz because of a build-in inductance, but it does not affect the overall performance. As can be seen, however, the experimental frequency response indicates a 3-dB cut-off frequency around 8 GHz, which is consistent with RC estimation. The cause for a RC limited modulation bandwidth is possibly due to the large radio frequency (RF) propagation loss introduced from low conductive p cladding layer, and the details will be explained in the discussions. Regardless, 8-GHz bandwidth is still sufficient for 10-Gb/s data transmission. The 10-Gb/s eye diagram of this modulator is depicted in the inset of Fig. 8(b) with −3.8-V bias and 1.5-V swing voltage while the other arm is adjusted to achieve the best signal quality. The signal has an ER of 6.3 dB, which is smaller than that measured at DC bias due to the partial voltage drop across the series resistance and cladding layer. The eye is clearly open and sufficient for 10-Gb/s operation. The noisy one level is due to the frequency overshoot at 1.4 GHz.

A 10-Gb/s bit-error-rate (BER) measurement is also performed to explore the sensitivity at all-port configurations of a switch. As illustrated in Fig. 9, all power penalties are below 0.5 dB at 10^{-10} BER and most important, no error floor is presented. Furthermore, the rise and fall time of the switch are around 50 ps between 10% and 90%, as depicted in the inset of Fig. 9, while the drive signal itself has a rise time around 70 ps. This indicates the potential use in a high speed switch or routing network for future high speed optical interconnects.

To investigate the power dependency of the MZM, a MZM is tested under different exposure intensities. Figure 10 shows the transmission curve for different input power levels. All three curves in Fig. 10 have a highest transmission at bias other than zero due to fabrication imperfections. The voltage-length product decreases from 1.95 to 1 V·mm as the input power increases from −7.5 to 12.5 dBm. The reduction in voltage-length product can be attributed to the excess carriers generated by two-photon absorption (TPA) at higher optical intensity. The shift of the peak point to higher reverse bias voltage also indicates the increase of free carriers in where a stronger electrical field is required to deplete the MQW/SCH region. The DC modulation response depends on the input optical power level, but the microwave modulation response is unaffected because the frequency range is much higher than the response time of the carriers (carrier lifetime in nanoseconds level) generated by TPA. To reduce this difference, the band gap

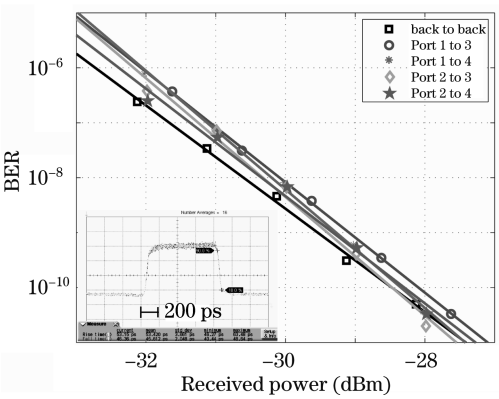

Fig. 9. BER versus received optical power for all-port configurations at 10 Gb/s with $2^{31}-1$ non-return-to-zero (NRZ) PRBS. Inset is the response of rise and fall time measured by 10% and 90% with 200 ps/div.

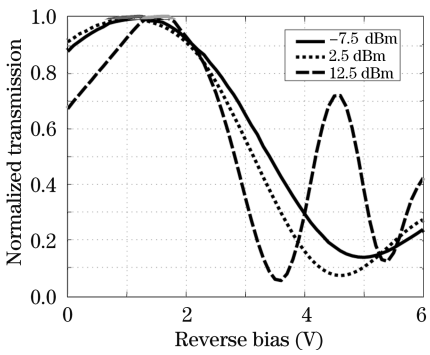

Fig. 10. Normalized transmission as a function of reverse bias of a MZM with different input power levels.

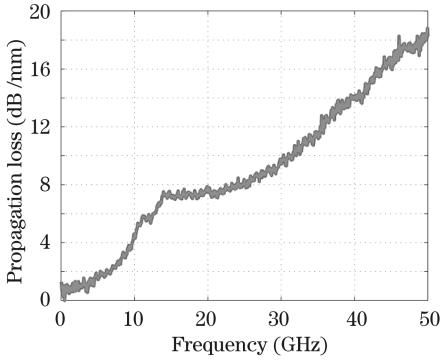

Fig. 11. RF propagation loss at different frequencies of a 500-μm CPW electrode.

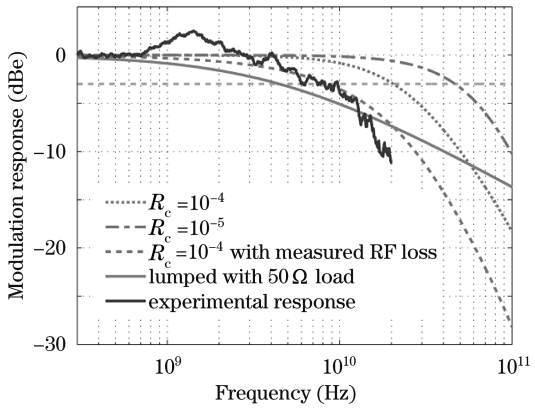

Fig. 12. Calculated modulation response for a 500-μm-long MZM using quasi-static equivalent circuit model.

and doping of the QW can be redesigned to decrease the carrier lifetime such that the contribution of index change from TPA can be reduced if high speed operation is required.

RF propagation loss is an issue when the TWE design is considered to implement on the device. The electromagnetic wave propagating along the waveguide decays dramatically when low conductive materials are nearby. For example, the cladding layer used for the depletion modulator has a conductivity of 2400 S/m, relatively small compared with metals, and this corresponds to a skin depth around 100 μm at 10 GHz, which is much larger than the mesa dimension. Therefore, fields will penetrate into the semiconductor and experience extra loss when the electromagnetic wave propagates along the device. To get the approximate propagation loss of the CPW, a full two-port S parameter was measured and converted to $ABCD$ matrix. The device characteristic impedance of 20 Ω and the propagation loss, shown in Fig. 11, were then calculated using the formula listed in Ref. [16]. As expected, the propagation loss increases with frequency because the attenuation coefficient is proportional to both operating frequency and conductivity. The loss is around 6 dB/mm at 10 GHz and increases to 14 dB/mm at 40 GHz. For a typical hybrid MZM with the length between 500−1000 μm, the electrical signal has a significant decay and thus results in insufficient modulation along the device. In consequence, this loss degrades the high speed performance even though a TWE is present.

Figure 12 shows the calculated response for a 500-μm-long MZM modulator using quasi-static equivalent circuit model[17] and lumped element analysis. The model covers voltage loss over series resistance, velocity mismatch, and RF loss from the transmission line. The missing factor in the modeling is the reflection loss due to impedance mismatch between RF source and TWE. The high RF propagation loss limits the bandwidth to less than 10 GHz while the model predicts that it is capable of operation up to 20 GHz. To overcome this problem, another TWE design such as capacitance loading technique is necessary in the future[18]. By utilizing the capacitance loading TWE, the fields can be pulled away from the III-V mesa structure so that the loss can be significantly reduced while T loading sections provide essential bias to deplete the carriers[18]. Moreover, the period of the loading sections and the filling factor can be adjusted to match the electrical phase velocity and optical signal for better modulation efficiency. The 20 GHz limitation comes from our high contact resistance R_c, especially of the p-contact on top of the narrow mesa, which is around 10^{-4} Ω·cm^2. By reducing one order of magnitude of the contact resistance, a 500-μm-long MZM is capable of 40-GHz modulation with proper termination.

In conclusion, we have successfully demonstrated high speed EAM, MZM, and switches on the hybrid silicon evanescent platform. The EAM has a modulation bandwidth as high as 16 GHz with 10-dB ER at −5 V. By manipulating the undercut of the mesa structure, the trade-off between bandwidth and efficiency can be achieved based on different requirements. A MZM utilizing the carrier depletion effect has a $V_\pi L$ of 2 V·mm, an optical bandwidth of 150 nm, and operation speed up to 10 Gb/s with 6.3-dB ER and 1.5-V driving voltage. The hybrid switch exhibits low power penalty of 0.5 dB for all-port configurations with 10-Gb/s data stream. Its rise and fall time, which is about 50 ps, indicates the capability for low overhead, low latency, high speed switching. The hybrid silicon evanescent modulators and switches can be used for optical interconnects and further integrated with other optical devices to achieve a transparent optical communication system.

The authors thank Alex Fang, Hyundai Park, and Di Liang for useful discussions on fabrication and Matt Sysak for the initial idea of using carrier depletion in the modulator. The authors also thank Matt Dummer for helpful suggestions on RF design, John Mack for BER testing, and J. Shah for supporting this project. This work was under the financial support from DARPA/MTO and ARL, USA.

References

1. A. Liu, R. Jones, L. Liao, D. Samara-Rubio, D. Rubin, O. Cohen, R. Nicolaescu, and M. Paniccia, Nature **427,** 615 (2004).
2. D. Marris-Morini, X. Le Roux, L. Vivien, E. Cassan, D. Pascal, M. Halbwax, S. Maine, S. Laval, J. M. Fédéli, and J. F. Damlencourt, Opt. Express **14,** 10838 (2006).
3. Y. Jiang, W. Jiang, L. Gu, X. Chen, and R. T. Chen, Appl. Phys. Lett. **87,** 221105 (2005).
4. Q. Xu, B. Schmidt, S. Pradhan, and M. Lipson, Nature **435,** 325 (2005).
5. R. S. Jacobsen, K. N. Andersen, P. I. Borel, J. Fage-Pedersen, L. H. Frandsen, O. Hansen, M. Kristensen,

A. V. Lavrinenko, G. Moulin, H. Ou, C. Peucheret, B. Zsigri, and A. Bjarklev, Nature **441,** 199 (2006).
6. J. E. Roth, O. Fidaner, R. K. Schaevitz, Y.-H. Kuo, T. I. Kamins, J. S. Harris, Jr., and D. A. B. Miller, Opt. Express **15,** 5851 (2007).
7. J. Liu, M. Beals, A. Pomerene, S. Bernardis, R. Sun, J. Cheng, L. C. Kimerling, and J. Michel, Nature Photon. **2,** 433 (2008).
8. M. N. Sysak, J. O. Anthes, J. E. Bowers, O. Raday, and R. Jones, Opt. Express **16,** 12478 (2008).
9. H. Fukano, T. Yamanaka, M. Tamura, and Y. Kondo, J. Lightwave Technol. **24,** 2219 (2006).
10. H.-W. Chen, Y.-H. Kuo, and J. E. Bowers, IEEE Photon. Technol. Lett. **20,** 1920 (2008).
11. G. Bastard, E. E. Mendez, L. L. Chang, and L. Esaki, Phys. Rev. B **28,** 3241 (1983).
12. J. G. Mendoza-Alvarez, L. A. Coldren, A. Alping, R. H. Yan, T. Hausken, K. Lee, and K. Pedrotti, J. Lightwave Technol. **6,** 793 (1988).
13. J.-F. Vinchant, J. A. Cavailles, M. Erman, P. Jarry, and M. Renaud, J. Lightwave Technol. **10,** 63 (1992).
14. D. Liang and J. E. Bowers, J. Vac. Sci. Technol. B **26,** 1560 (2008).
15. H. Park, Y.-H. Kuo, A. W. Fang, R. Jones, O. Cohen, M. J. Paniccia, and J. E. Bowers, Opt. Express **15,** 13539 (2007).
16. K. Kiziloglu, N. Dagli, G. L. Matthaei, and S. I. Long, IEEE Trans. Microwave Theory Tech. **39,** 1361 (1991).
17. G. L. Li, C. K. Sun, S. A. Pappert, W. X. Chen, and P. K. L. Yu, IEEE Trans. Microwave Theory Tech. **47,** 1177 (1999).
18. J. Shin, C. Ozturk, S. R. Sakamoto, Y. J. Chiu, and N. Dagli, IEEE Trans. Microwave Theory Tech. **53,** 636 (2005).